



# 1 Air pollution satellite-based CO<sub>2</sub> emission inversion: system 2 evaluation, sensitivity analysis, and future perspective

3 Hui Li<sup>1,2</sup>, Jiaxin Qiu<sup>1,2</sup>, Bo Zheng<sup>1,2,\*</sup>

4 <sup>1</sup>Shenzhen Key Laboratory of Ecological Remediation and Carbon Sequestration, Institute of Environment  
5 and Ecology, Tsinghua Shenzhen International Graduate School, Tsinghua University, Shenzhen 518055,  
6 China.

7 <sup>2</sup>State Environmental Protection Key Laboratory of Sources and Control of Air Pollution Complex, Beijing  
8 100084, China.

9 Correspondence to: Bo Zheng ([bozheng@sz.tsinghua.edu.cn](mailto:bozheng@sz.tsinghua.edu.cn))

10 **Abstract.** Simultaneous monitoring of greenhouse gases and air pollutant emissions is crucial for combating  
11 global warming and air pollution to prevent irreversible damage. We previously established an air pollution  
12 satellite-based carbon dioxide (CO<sub>2</sub>) emission inversion system, successfully capturing CO<sub>2</sub> and nitrogen  
13 oxides (NO<sub>x</sub>) emission fluctuations amid socioeconomic changes. However, the system's robustness and  
14 weaknesses have not yet been fully evaluated. Here, we conduct a comprehensive sensitivity analysis with  
15 31 tests on various factors including prior, model resolution, satellite constraint, and inversion system  
16 configuration to assess the vulnerability of emission estimates across temporal, sectoral, and spatial  
17 dimensions. The Relative Change (*RC*) between these tests and Base inversion reflects the different  
18 configurations' impact on inferred emissions, with one standard deviation ( $1\sigma$ ) of *RC* indicating consistency.  
19 Although estimates show increased sensitivity to tested factors at finer scales, the system demonstrates  
20 notable robustness, especially for annual national total NO<sub>x</sub> and CO<sub>2</sub> emissions across most tests ( $RC < 4.0\%$ ).  
21 Spatiotemporally diverse changes in parameters tend to yield inconsistent impacts ( $1\sigma \geq 4\%$ ) on estimates,  
22 and vice versa ( $1\sigma < 4\%$ ). The model resolution, satellite constraint, and NO<sub>x</sub> emission factors emerge as the  
23 major influential factors, underscoring their priority for further optimization. Taking daily national total CO<sub>2</sub>  
24 emissions as an example,  $\overline{RC} \pm 1\sigma$  they incur can reach  $-1.2 \pm 6.0\%$ ,  $1.3 \pm 3.9\%$ , and  $10.7 \pm 0.7\%$ , respectively.  
25 This study reveals the robustness and areas for improvement in our air pollution satellite-based CO<sub>2</sub> emission  
26 inversion system, offering opportunities to enhance the reliability of CO<sub>2</sub> emission monitoring in the future.

## 27 1 Introduction

28 The knowledge of emissions, i.e., how much and where pollutants are released into the atmosphere, lays the  
29 foundation for understanding the changes in atmospheric compositions and managing emissions toward  
30 climate and air quality targets (Meinshausen et al., 2022; Li et al., 2022; Zhang et al., 2019). Anthropogenic  
31 emissions are strongly modulated by socioeconomic events (e.g., holidays, economic recession, and  
32 recovery), therefore, it is essential to monitor emissions timely to interpret atmospheric species  
33 concentrations (Shan et al., 2021; Le Quéré et al., 2021; Guevara et al., 2023). Currently, numerous nations,



34 particularly those within the Global South (i.e., China), grapple with the dual imperatives of mitigating air  
35 pollution and addressing climate change challenges. To effectively navigate these intertwined challenges in  
36 a harmonized and resource-efficient manner, the development of a system capable of disentangling variations  
37 in emissions and their driving factors for greenhouse gases and air pollutants is indispensable (Ke et al., 2023).

38 Recently, a discernible trend is emerging towards inferring anthropogenic carbon dioxide (CO<sub>2</sub>) emissions  
39 from well-observed and co-emitted air pollutants (i.e., nitrogen dioxide, NO<sub>2</sub>) given their co-emission  
40 characteristics in time and space (Wren et al., 2023; Yang et al., 2023; Liu et al., 2020a; Reuter et al., 2019).  
41 The introduction of NO<sub>2</sub> in the CO<sub>2</sub> emission estimation presents several distinct advantages. NO<sub>2</sub> has a short  
42 lifetime of several hours, rendering its source-contributing plumes readily detectable via remote sensing  
43 techniques, thus facilitating their inversion into emission estimates (Goldberg et al., 2019). In contrast, the  
44 longevity of CO<sub>2</sub>, spanning hundreds of years, combined with its elevated background concentration reaching  
45 hundreds of parts per million (ppm), obscures the detection of local source-triggered concentration  
46 enhancements (i.e., several ppm) (Nassar et al., 2017; Reuter et al., 2019). Moreover, the advancement of  
47 remote sensing technologies for NO<sub>2</sub> has surpassed the progress in CO<sub>2</sub> satellite observations, as evidenced  
48 by the increased frequency of satellite revisits, enhanced pixel spatial resolution, broader coverage, and  
49 improved signal-to-noise ratio in column concentration observation (Macdonald et al., 2023; Cooper et al.,  
50 2022). The synergistic quantification of CO<sub>2</sub> and nitrogen oxides (NO<sub>x</sub>) emissions has gained substantial  
51 attention, not to mention that it could provide valuable guidance for a joint effort to monitor and mitigate air  
52 pollutants and carbon emissions concurrently (Miyazaki and Bowman, 2023).

53 We have developed an air pollution satellite sensor-based CO<sub>2</sub> emission inversion system, which is capable  
54 of concurrently estimating ten-day moving average sector-specific anthropogenic NO<sub>x</sub> and CO<sub>2</sub> emissions by  
55 integrating top-down and bottom-up methods. This integrated methodology has proven effective in capturing  
56 emission fluctuations, particularly during the coronavirus disease 2019 (COVID-19) pandemic (Zheng et al.,  
57 2020; Li et al., 2023). While previous sensitivity tests have suggested a certain level of accuracy, the system  
58 has not yet undergone a comprehensive evaluation to thoroughly assess its robustness and weaknesses, and  
59 thereby clearly imply its future developmental trajectory. To bridge this gap, we here undertake an extensive  
60 sensitivity analysis with 31 tests using the 2022 anthropogenic NO<sub>x</sub> and CO<sub>2</sub> emission estimation as a case  
61 study. Our analytical endeavor delves into how emission outcomes respond to a variety of sensitivity  
62 assessments across temporal, sectoral, and spatial dimensions. This study aims to diagnose and rank the  
63 uncertainty sources, providing insights to prioritize improvements of this inversion system in the future.

## 64 **2 Materials and methods**

65 Our air pollution satellite sensor-based CO<sub>2</sub> emission inversion system has been elucidated in our previous  
66 studies (Zheng et al., 2020; Li et al., 2023). In essence, this system integrates top-down and bottom-up data  
67 streams to infer the ten-day moving average anthropogenic NO<sub>x</sub> and CO<sub>2</sub> emissions by sector in China based  
68 on the mass-balance approach (Cooper et al., 2017). Comprising three key components, the system involves



69 the bottom-up inference of prior emissions for NO<sub>x</sub> and CO<sub>2</sub> with sectoral profile, the top-down estimation  
 70 of total NO<sub>x</sub> emissions constrained by satellite observation, and the integration of both sources to derive  
 71 satellite-constrained NO<sub>x</sub> and CO<sub>2</sub> emissions by sector (Fig. S1). Each of these processes could introduce  
 72 uncertainties in the final emission estimates. To assess the potential uncertainties, we establish a baseline  
 73 (Base) for emissions computed using our conventional settings (Li et al., 2023; Zheng et al., 2020) and further  
 74 investigate sensitivity tests to characterize the impacts of the different configurations on final estimates.

## 75 2.1 Base inversion

76 In the Base inversion, we adhered to the same parameters and configurations outlined in previous studies for  
 77 estimating the ten-day moving average anthropogenic NO<sub>x</sub> and CO<sub>2</sub> emissions by sector in 2022 (Table 1)  
 78 (Li et al., 2023; Zheng et al., 2020). Succinctly, we first updated sectoral NO<sub>x</sub> and CO<sub>2</sub> emissions through  
 79 the bottom-up process. This involved utilizing indicators including industrial production, thermal power  
 80 generation, freight turnover, and population-weighted heating degree days as proxies for changes in industry,  
 81 power, transport, and residential activity levels. Secondly, we inferred the total anthropogenic NO<sub>x</sub> emissions  
 82 constrained by TROPospheric Monitoring Instrument (TROPOMI) NO<sub>2</sub> retrievals (v2.4) (Van Geffen et al.,  
 83 2022). A critical step in this process was establishing a relationship between NO<sub>2</sub> tropospheric vertical  
 84 column densities (TVCDs) and anthropogenic NO<sub>x</sub> emissions (Eq. 1) through GEOS-Chem simulation  
 85 (v12.3.0, <https://geoschem.github.io/>) at a horizontal resolution of 0.5°×0.625°. Our analysis focused on the  
 86 grids where anthropogenic emissions prevail (Liu et al., 2020b), characterized by ten-day moving average  
 87 NO<sub>2</sub> TVCDs exceeding 1×10<sup>15</sup> molecules cm<sup>-2</sup>. Thirdly, we integrated the bottom-up and top-down data  
 88 flows to yield TROPOMI-constrained sectoral NO<sub>x</sub> emissions. Assuming that each grid's emission variability  
 89 was primarily driven by its dominant source sectors (contributing over 50%), we utilized the discrepancy  
 90 between the bottom-up and top-down estimates in grid cells dominated by a particular sector to derive sector-  
 91 specific scaling factors, which were subsequently applied to correct the bottom-up sectoral NO<sub>x</sub> emissions.  
 92 Following this adjustment, we rescaled the corrected bottom-up emissions to ensure alignment with the  
 93 TROPOMI-constrained total emissions. Finally, we converted the sectoral NO<sub>x</sub> emissions to corresponding  
 94 CO<sub>2</sub> emissions with the CO<sub>2</sub>-to-NO<sub>x</sub> emission ratios derived from the bottom-up process (Eq. 4).

$$95 \quad E_{t,i,TROPOMI,y} = (1 + \beta_{t,i}) \left( \frac{\Delta\Omega}{\Omega} \right)_{t,i,anth,y} \times E_{t,i,bottom-up,2019} \quad (1)$$

$$96 \quad \beta_{t,i} = \frac{\Delta E_{t,i,bottom-up,2019}}{E_{t,i,bottom-up,2019}} \div \frac{\Omega_{t,i,40\%emi,2019} - \Omega_{t,i,base,2019}}{\Omega_{t,i,base,2019}} \quad (2)$$

$$97 \quad \left( \frac{\Delta\Omega}{\Omega} \right)_{t,i,anth,y} = \frac{\Omega_{t,i,sate,y}}{\Omega_{t,i,sate,2019}} - \frac{\Omega_{t,i,simu\_fixemis,y}}{\Omega_{t,i,simu,2019}} \quad (3)$$

$$98 \quad C_{s,i,TROPOMI,y} = E_{s,i,TROPOMI,y} \times \frac{EF_{CO_2s,i,bottom-up,2019}}{EF_{NO_x s,i,bottom-up,2019} \times (1 - rNO_{xs,i,y})} \quad (4)$$

99 Where  $t$ ,  $i$ , and  $y$  represent the ten-day window, model grid cell (i.e., 0.5°×0.625°), and target year 2022,  
 100 respectively.  $E_{t,i,TROPOMI,y}$  is the anthropogenic total NO<sub>x</sub> emissions constrained by TROPOMI NO<sub>2</sub> TVCDs.



101  $E_{t,i,\text{bottom-up},2019}$  is the anthropogenic NO<sub>x</sub> emissions in 2019 from the Multi-resolution Emission Inventory for  
 102 China (MEIC) inventory (Zheng et al., 2018).  $\beta_{t,i}$  is a unitless factor relating the changes in NO<sub>2</sub> TVCDs to  
 103 anthropogenic NO<sub>x</sub> emissions (Lamsal et al., 2011).  $\Delta E_{t,i,\text{bottom-up},2019}/E_{t,i,\text{bottom-up},2019}$  represent the implemented  
 104 40% reduction in anthropogenic NO<sub>x</sub> emissions over China.  $\Omega_{t,i,-40\%\text{emi},2019}$  and  $\Omega_{t,i,\text{base},2019}$  are GEOS-Chem  
 105 simulated NO<sub>2</sub> TVCDs at the TROPOMI overpass time in 2019 with a 40% emission reduction and without  
 106 any emission reduction, respectively.  $(\Delta\Omega/\Omega)_{t,i,\text{anth},y}$  refers to the relative changes in NO<sub>2</sub> TVCDs due to  
 107 anthropogenic NO<sub>x</sub> emission changes between 2019 and 2022.  $\Omega_{t,i,\text{state},y}/\Omega_{t,i,\text{state},2019}$  indicates the relative  
 108 differences in TROPOMI NO<sub>2</sub> TVCDs between 2019 and 2022, and  $\Omega_{t,i,\text{simu\_fixemis},y}/\Omega_{t,i,\text{simu},2019}$  represents the  
 109 relative changes in NO<sub>2</sub> TVCDs caused by inter-annual meteorological variation, which are derived from  
 110 GEOS-Chem simulations with the fixed 2019 emissions and meteorological field in target year. In Eq. 4,  
 111  $C_{s,i,i,\text{TROPOMI},y}$  and  $E_{s,i,i,\text{TROPOMI},y}$  are CO<sub>2</sub> and NO<sub>x</sub> emissions from sector  $s$ .  $EF_{\text{CO}_2,s,i,\text{bottom-up},2019}$  and  $EF_{\text{NO}_x}$   
 112  $_{s,i,\text{bottom-up},2019}$  are the sectoral emission factors (EFs) of CO<sub>2</sub> and NO<sub>x</sub> in 2019 derived from the MEIC emission  
 113 model.  $r\text{NO}_x_{s,i,y}$  is the reduction in NO<sub>x</sub> EFs by sector from 2019 to 2022 derived from the bottom-up  
 114 estimation, while the CO<sub>2</sub> EFs are assumed to remain unchanged.

115 We approximate the annual NO<sub>x</sub> and CO<sub>2</sub> emissions as the sum of the ten-day moving average NO<sub>x</sub> and CO<sub>2</sub>  
 116 emissions in 2022 with a vacancy in the first and last five days. This approximation, however, does not impact  
 117 our analysis, as our primary objective is to identify potential sources of uncertainty within the system and  
 118 thereby highlight areas for future improvement.

119 **Table 1. Configurations of Base inversion.**

Factors/parameters	Base setting
GEOS-Chem (GC) resolution	GEOS-Chem simulation with the resolution of 0.5°×0.625°
TROPOMI retrievals version	v2.4 of TROPOMI NO <sub>2</sub>
TROPOMI screening schemes	Cloud fraction (CF)<0.4, quality flag (QA)>0.5
Reference year	2019
NO <sub>x</sub> emission factors (EFs)	The reduction ratio of NO <sub>x</sub> EFs halves annually
Threshold value to identify dominant emission source sectors for each grid	50%
Sectors in bottom-up estimation	8 sectors (power, industry, cement, iron, residential, residential-bio, on-road, and off-road)

120

## 121 2.2 Sensitivity inversion tests

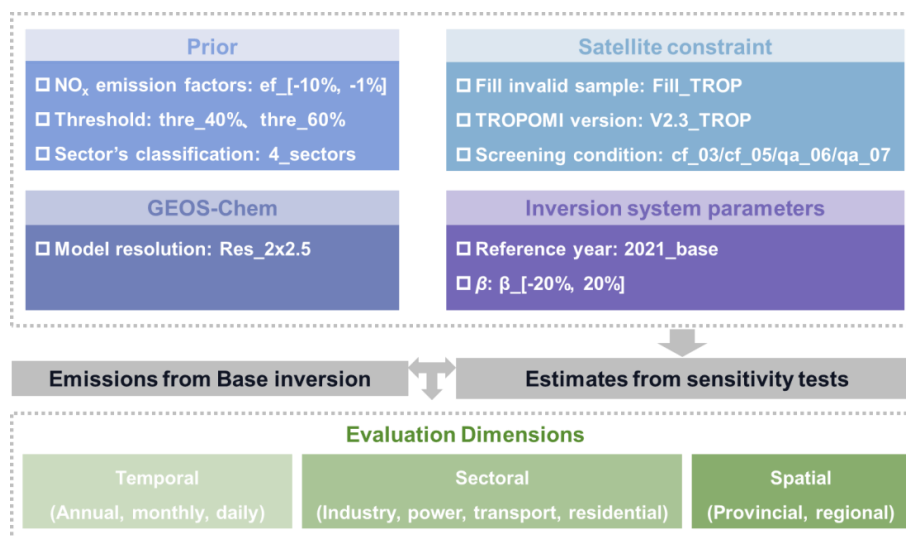
122 The sensitivity inversion experiments consist of 31 tests concerning factors encompassing prior, model  
 123 resolution, satellite constraint, and inversion system parameters to achieve a comprehensive evaluation of the  
 124 system (Fig. 1 and Table 2). Each test is conducted as a controlled experiment, where only one parameter is  
 125 altered while the rest remain the same as their Base inversion setting.



126 **Table 2. Settings of 31 sensitivity inversion tests.**

Category	Num	Name	Settings description	Test objectives
GC	1	Res_2x2.5	GEOS-Chem simulation with the resolution of 2°x2.5°	Model resolution
	2	Trop_fill	Complementing TROPOMI NO <sub>2</sub> with machine learning	Sampling coverage
Satellite constraint	3	Trop_v2.3	Substituting TROPOMI NO <sub>2</sub> from v2.4 to v2.3	Satellite data version
	4	Trop_cf03	Changing CF limit from 0.4 to 0.3	Satellite data filtering condition
	5	Trop_cf05	Changing CF limit from 0.4 to 0.5	
	6	Trop_qa06	Changing QA limit from 0.5 to 0.6	
	7	Trop_qa07	Changing QA limit from 0.5 to 0.7	
Inversion system parameters	8	2021_base	Changing the reference year from 2019 to 2021	Reference year
	9	β_-20%	Scaling β down by 20%	β
	10	β_-15%	Scaling β down by 15%	
	11	β_-10%	Scaling β down by 10%	
	12	β_-5%	Scaling β down by 5%	
	13	β_-1%	Scaling β down by 1%	
	14	β_1%	Scaling β up by 1%	
	15	β_5%	Scaling β up by 5%	
	16	β_10%	Scaling β up by 10%	
	17	β_15%	Scaling β up by 15%	
18	β_20%	Scaling β up by 20%		
Prior	19	ef_-10%	Scaling changes in NO <sub>x</sub> EFs down by 10%	NO <sub>x</sub> EFs
	20	ef_-9%	Scaling changes in NO <sub>x</sub> EFs down by 9%	
	21	ef_-8%	Scaling changes in NO <sub>x</sub> EFs down by 8%	
	22	ef_-7%	Scaling changes in NO <sub>x</sub> EFs down by 7%	
	23	ef_-6%	Scaling changes in NO <sub>x</sub> EFs down by 6%	
	24	ef_-5%	Scaling changes in NO <sub>x</sub> EFs down by 5%	
	25	ef_-4%	Scaling changes in NO <sub>x</sub> EFs down by 4%	
	26	ef_-3%	Scaling changes in NO <sub>x</sub> EFs down by 3%	
	27	ef_-2%	Scaling changes in NO <sub>x</sub> EFs down by 2%	
	28	ef_-1%	Scaling changes in NO <sub>x</sub> EFs down by 1%	
	29	thre_40%	Changing the dominant sector threshold from 50% to 40%	Threshold
	30	thre_60%	Changing the dominant sector threshold from 50% to 60%	
	31	4_sectors	Aggregating the sectors from 8 to 4 in prior estimates	Sector's classification

127



128

129

130

**Figure 1. Overview of the sensitivity inversion tests in this study.** Details of the processes and settings are presented in Fig. S1 and Table 2.

131

### 2.2.1 Prior emission inventory

132

The prior provides the sectoral profile for subsequent emission attribution. We conducted a comprehensive examination of associated parameters, including NO<sub>x</sub> EFs influencing the conversion of NO<sub>x</sub> to CO<sub>2</sub> emissions by sector, threshold value defining the dominant sector for each grid, and sector classification. For NO<sub>x</sub> EFs settings, we devised a ten-level gradient ranging from -10% to -1% (referred to as ef\_<sub>[-10%, -1%]</sub>). Regarding the threshold value, we varied it from 50% to 40% and 60% (referred to as thre\_<sub>40%</sub> and thre\_<sub>60%</sub>), respectively. For sector classification, the original prior NO<sub>x</sub> and CO<sub>2</sub> emissions were updated based on eight sectors in the bottom-up process: power, industry, cement, iron, residential, residential-bio, on-road, and off-road. This detailed sectoral structure facilitates relatively detailed bottom-up estimations with specific sectoral activity levels. These eight sectors were then aggregated into four categories: power, industry (sum of original industry, cement, and iron), residential (sum of original residential and residential-bio), and transport (sum of original on-road and off-road) when allocating TROPOMI-constrained total NO<sub>x</sub> emissions into sectors. Here, this sector consolidation, specifically implemented before the bottom-up estimation (4\_sectors), was designed to evaluate the influence of sector classification on the inversion results.

145

### 2.2.2 GEOS-Chem model resolution

146

The model resolution of the GEOS-Chem simulation inherently shapes the localized relationship between NO<sub>2</sub> TVCDs and NO<sub>x</sub> emissions established in the top-down process. Finer resolution is advantageous for establishing localized connections between air pollutant emissions and atmospheric concentrations, and the attribution of sectoral emissions. However, excessively fine resolution is not applicable due to the inter-grid transport when employing the mass-balance method (Turner et al., 2012). To explore the impact of resolution

147

148

149

150



151 on emission estimates, we performed an inversion experiment with simulations at a coarser resolution of  
152  $2^{\circ} \times 2.5^{\circ}$  (Res\_2x2.5).

### 153 **2.2.3 Satellite constraint**

154 The TROPOMI NO<sub>2</sub> retrievals serve as a constraint in the top-down NO<sub>x</sub> emission estimation. We conducted  
155 experiments on the TROPOMI NO<sub>2</sub> retrievals through three distinct approaches. Firstly, we used Extreme  
156 Gradient Boosting (XGBoost) to fill the invalid satellite retrievals in v2.4 TROPOMI (Trop\_fill) by  
157 establishing relationships between TROPOMI NO<sub>2</sub> TVCDs and meteorological variables, as well as GEOS-  
158 Chem simulated NO<sub>2</sub> TVCDs (modeled\_NO<sub>2</sub> in Eq. 5) (Wei et al., 2022). The meteorological variables were  
159 derived from European Centre for Medium-Range Weather Forecasts (ECMWF) ERA5 dataset (Hersbach et  
160 al., 2020), including boundary layer height (BLH), surface pressure (SP), temperature (TEM), dewpoint  
161 temperature (DT), 10m u-component (WU), 10m v-component of winds (WV), total precipitation (TP),  
162 evaporation (EP), downward uv radiation at the surface (surUV), and mean surface downward uv radiation  
163 flux (downUV). In the XGBoost process, we trained the relationship for daily NO<sub>2</sub> TVCDs throughout the  
164 year grid-by-grid, with 80% of the data used as the training set and 20% as the test set.

$$165 \quad \text{TROPOMI\_NO}_2 \sim f_{\text{XGBoost}}(\text{modeled\_NO}_2, \text{BLH}, \text{SP}, \text{TEM}, \text{DT}, \text{WU}, \text{WV}, \text{TP}, \text{EP}, \text{surUV}, \text{downUV}) \quad (5)$$

166 The comparison of NO<sub>2</sub> TVCDs before and after data filling revealed minimal impact from the original  
167 missing data (Fig. S2). This is attributed to our system's utilization of a ten-day moving average of NO<sub>2</sub>  
168 TVCDs, which effectively mitigates the influence of missing data at the grid scale.

169 Secondly, we evaluated the impact of different versions of TROPOMI NO<sub>2</sub> retrievals by substituting the v2.4  
170 TROPOMI data with the older v2.3 TROPOMI NO<sub>2</sub> columns (Trop\_v2.3). Updates in TROPOMI data  
171 products generally help address the low bias of NO<sub>2</sub> concentrations, particularly in heavily polluted regions  
172 (Lange et al., 2023; Van Geffen et al., 2022). Thirdly, we adjusted the satellite data screening policies to  
173 investigate the uncertainties associated with satellite observations on emission estimates, which involved  
174 varying the cloud fraction (CF) limit to 0.3 (Trop\_cf03) or 0.5 (Trop\_cf05) and modifying the quality flag  
175 (QA) limit to 0.6 (Trop\_qa06) or 0.7 (Trop\_qa07), respectively. CF and QA serve as crucial parameters in  
176 screening applicable NO<sub>2</sub> TVCDs, representing primary sources of uncertainty in satellite observations (Van  
177 Geffen et al., 2022; Lange et al., 2023).

### 178 **2.2.4 Inversion system parameters**

179 In previous studies, the reference year for updating emissions for target years was 2019. Here, we modified  
180 the reference year to 2021 (2021\_base) to assess its impact. The parameter  $\beta$  represents the localized  
181 relationship between changes in NO<sub>2</sub> TVCDs and changes in anthropogenic NO<sub>x</sub> emissions (Eq. 2),  
182 determining the transition from observed changes in NO<sub>2</sub> TVCDs to changes in anthropogenic NO<sub>x</sub> emissions  
183 in the top-down process (Eq. 1). To explore potential nonlinear responses in the estimated results to this  
184 parameter, we devised a ten-level gradient for  $\beta$ , ranging from -20% to 20% (refer to as  $\beta_{[-20\%, 20\%]}$ ).



185 **2.3 Evaluation of different configurations' impact**

186 The sensitivity analysis of the NO<sub>x</sub> and CO<sub>2</sub> emissions estimated by our inversion system has illuminated  
 187 potential sources of uncertainty and the magnitude of their impacts. To quantify the influence of sensitivity  
 188 tests on emission estimates, we calculated the Relative Change (*RC*) between emissions estimated under  
 189 different tests and the Base inversion, and one standard deviation ( $1\sigma$ ) of *RC* to evaluate the consistency of  
 190 their impact across temporal, sectoral, and spatial scales (details seen in Table 3). It is noteworthy that on the  
 191 annual national total emission scale (maximization of all three dimensions), the value of  $1\sigma$  equals 0.0%.

192 **Table 3. Calculation of *RC* and  $1\sigma$  across different dimensions.**

Dimension	Equations	Parameters
Temporal	$RC_t = \frac{E_{t,sensi} - E_{t,base}}{E_{t,base}}$ $\sigma_t = \sqrt{\frac{\sum_i^n (RC_i - \overline{RC_t})^2}{n}}$	<ul style="list-style-type: none"> <li>• <i>t</i> represents timescale, denoting year, month, or ten-day window.</li> <li>• <math>E_{t,sensi}</math> and <math>E_{t,base}</math> denote the national total emissions under a specific sensitivity test and Base on corresponding temporal scale <i>t</i>.</li> <li>• <math>RC_t</math> and <math>\sigma_t</math> indicate the <i>RC</i> and its <math>1\sigma</math> of national total emissions across temporal scales. The <math>\sigma_t</math> equals 0.0% when <i>t</i> is the yearly scale.</li> </ul>
Sectoral	$RC_{t,s} = \frac{E_{t,s,sensi} - E_{t,s,base}}{E_{t,s,base}}$ $\sigma_s = \sqrt{\frac{\sum_t^n (RC_s - \overline{RC_s})^2}{n}} \text{ (Daily)}$	<ul style="list-style-type: none"> <li>• <i>s</i> represents sector source.</li> <li>• <math>E_{t,s,sensi}</math> and <math>E_{t,s,base}</math> refer to national sectoral emissions under sensitivity test and Base on temporal scale <i>t</i> (annual and daily).</li> <li>• <math>RC_{t,s}</math> indicates the <i>RC</i> of national sectoral emissions on a temporal scale <i>t</i>.</li> <li>• <math>\sigma_s</math> indicates <math>1\sigma</math> of <i>RC</i> of national sectoral emissions on a daily scale.</li> </ul>
Spatial	$RC_{t,p/r} = \frac{E_{t,p/r,sensi} - E_{t,p/r,base}}{E_{t,p/r,base}}$ $\sigma_p = \sqrt{\frac{\sum_p^m (RC_p - \overline{RC_p})^2}{m}} \text{ (Annual)}$ $\sigma_r = \sqrt{\frac{\sum_t^n (RC_r - \overline{RC_r})^2}{n}} \text{ (Daily)}$	<ul style="list-style-type: none"> <li>• <i>p</i> and <i>r</i> represent province and region (i.e., provincial clusters), respectively.</li> <li>• <math>E_{t,p/r,sensi}</math> and <math>E_{t,p/r,base}</math> refer to provincial/regional total emissions under sensitivity test and Base on temporal scale <i>t</i> (annual and daily).</li> <li>• <math>RC_{t,p/r}</math> indicates the <i>RC</i> of provincial/regional total emissions on a temporal scale <i>t</i>.</li> <li>• <math>\sigma_p</math> indicates <math>1\sigma</math> of <i>RC</i> of annual total emissions on the provincial scale.</li> <li>• <math>\sigma_r</math> indicates <math>1\sigma</math> of <i>RC</i> of regional total emissions on a daily scale.</li> </ul>

193

194 In this context, a condition where  $1\sigma$  is below 4.0% is deemed as a consistent impact on emission outcomes  
 195 within certain dimensions (the determination of 4.0% seen in Fig. S3). Conversely, when  $1\sigma$  exceeds or equals  
 196 4.0%, it is indicative of an inconsistent impact. For instance, a daily scale  $\sigma_t$  value of 6.2% in the Res\_2×2.5  
 197 test (Fig. S4) suggests that the model resolution exerts a temporally inconsistent influence on daily emission  
 198 estimates, whereas a daily scale  $\sigma_t = 0.0\%$  under ef\_-10% indicates temporal consistency in its influence.  
 199 These principles extend to other dimensions (i.e., sectoral and spatial). Factors whose sensitivity tests yield  
 200 large and inconsistent *RC* across finer time, sector, or region scales tend to introduce high uncertainty and





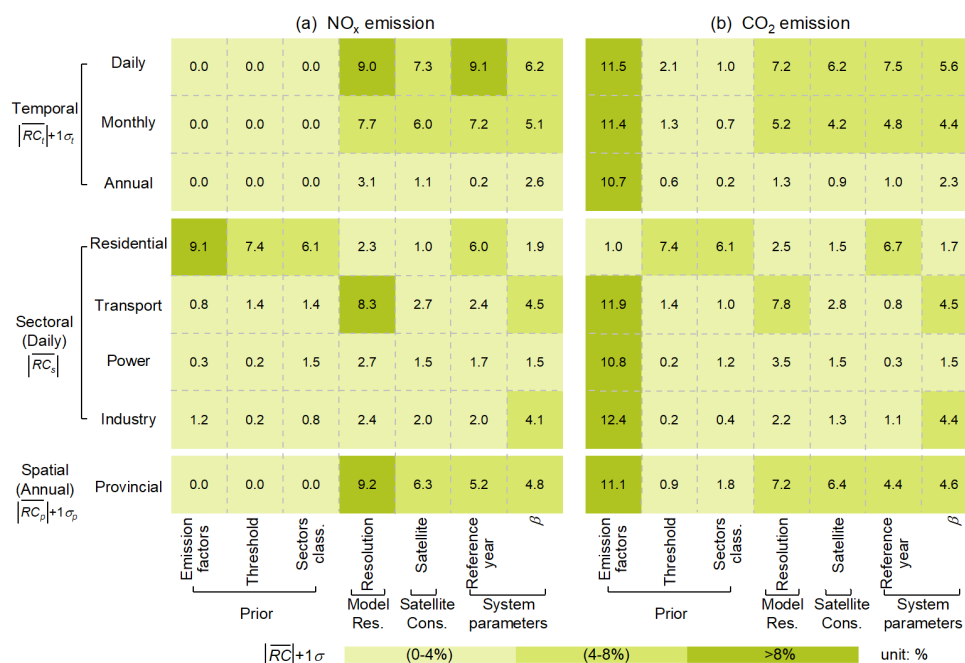
201 become a priority for future optimization. Conversely, small and consistent  $RC$  suggests sources with low  
202 uncertainty and a higher level of robustness in the system to those particular factors.

### 203 3 Results

#### 204 3.1 Overview of the emission responses to sensitivity tests

205 For a comprehensive understanding of emission sensitivity across various dimensions, we compute the sum  
206 of absolute average  $RC$  and  $1\sigma$  (i.e.,  $|\overline{RC}|+1\sigma$ ) to delineate potential most likely uncertainties associated with  
207 tested factors across spatial, temporal, and sectoral scales (Fig. 2). The impact of these tests on emissions are  
208 comparable between  $\text{NO}_x$  and  $\text{CO}_2$ , except for the  $\text{NO}_x$  EFs tests (first column in Fig. 2), which distinctly  
209 influence  $\text{NO}_x$  and  $\text{CO}_2$  emissions.  $\text{CO}_2$  emissions display high sensitivity to  $\text{NO}_x$  EFs across all dimensions  
210 compared to  $\text{NO}_x$  emissions, except in the residential sector where  $\text{NO}_x$  emissions are more responsive while  
211  $\text{CO}_2$  emissions are not. For instance,  $\text{ef}_{-10\%}$  (maximum reduction in  $\text{NO}_x$  EFs tests) incurs a  $|\overline{RC}|+1\sigma$  of  
212 10.7% in annual national  $\text{CO}_2$  emissions, with no corresponding impact on  $\text{NO}_x$  emissions. The relationship  
213 between annual national  $\text{CO}_2$  emissions and  $\text{NO}_x$  EFs exhibits linearity (Fig. S5), remaining within a 4.0%  
214 range if  $\text{NO}_x$  EFs reductions are kept below 4.0% (i.e.,  $\text{ef}_{[-4\%, -1\%]}$ ). In contrast, daily residential emissions  
215 show a  $|\overline{RC}|$  of only 1.0% in  $\text{CO}_2$  but up to 9.1% in  $\text{NO}_x$  emissions under the  $\text{ef}_{-10\%}$  test.

216 The remaining sensitivity tests, excluding the  $\text{NO}_x$  EFs, demonstrate comparable influences on both  $\text{NO}_x$  and  
217  $\text{CO}_2$  emissions (all columns except the first one). Among all dimensions examined, the annual national total  
218  $\text{NO}_x$  and  $\text{CO}_2$  emissions emerge as robust results, with a  $|\overline{RC}|+1\sigma$  of no more than 4.0% across tests. At a  
219 finer temporal scale (i.e., daily basis), the impacts of model resolution, reference year, and satellite constraint  
220 on estimated emissions are amplified, with their  $|\overline{RC}|+1\sigma$  tripling compared to the annual scale. This  
221 amplification primarily arises from the increased  $1\sigma$  on the daily scale (Fig. S4), indicating the substantial  
222 impact of these factors on daily emission estimates. At a finer spatial scale, provincial emissions are  
223 vulnerable to changes in model resolution, reference year, and satellite constraint due to their impacts'  
224 inconsistency in space (Fig. S4). Concerning sectoral emissions, industry and power sector emissions exhibit  
225 robustness, whereas transport and residential emissions present vulnerabilities to model resolution and  
226 dominant sector threshold value, respectively. In the following sections, we elaborate on the impacts of all  
227 sensitivity tests on  $\text{NO}_x$  and  $\text{CO}_2$  emissions from temporal, sectoral, and spatial perspectives. To clarify the  
228  $RC$  across different dimensions, we adopt  $RC_t$ ,  $RC_s$ , and  $RC_{p/r}$  to signify  $RC$  in temporal, sectoral, and spatial  
229 contexts, respectively.



230

231 **Figure 2. An overview of sensitivity inversion tests' impacts on (a) NO<sub>x</sub> and (b) CO<sub>2</sub> emissions.** The  
 232 color blocks in this figure represent the sum of absolute average  $RC$  and  $1\sigma$  (i.e.,  $|\overline{RC}|+1\sigma$ ), which reflect  
 233 the extent of the corresponding tests' impact. Sectoral and provincial results are depicted on an annual scale.  
 234 The numbers within each grid represent the maximum value of  $|\overline{RC}|+1\sigma$  under tests on corresponding factors.  
 235 For example, the  $|\overline{RC}|+1\sigma$  noted in the Emission factors column refers to  $ef_{-10\%}$ . It is noteworthy that the  
 236 sectoral dimensions in this figure display their absolute average  $RC$  on the daily scale, with their  
 237 corresponding  $1\sigma$  shown separately in Fig. S4.

### 238 3.2 Emission sensitivity at different temporal scales

239 To exclusively examine emission sensitivities in the temporal dimension, this section focuses on the variation  
 240 of national total emissions in each test. Tests influencing both NO<sub>x</sub> and CO<sub>2</sub> emissions exhibit comparable  
 241 effects, while prior tests exclusively influence CO<sub>2</sub> emissions (Fig. 3). For conciseness, we focus on the  $RC_t$   
 242 in CO<sub>2</sub> emissions in tests here (discussion on NO<sub>x</sub> emissions seen in Text. S1). The average  $RC_t$  of national  
 243 total emissions are comparable across temporal scales with differences below 1% (lines in Fig. 3, Figs. S6-  
 244 S7). However, the consistency of  $RC_t$  weakens from yearly to monthly to daily scales (increased  $1\sigma$  as shown  
 245 by the shadow in Fig. 3). To better characterize the extent of tests' impact, the discussion here focuses on the  
 246  $\overline{RC}_t \pm 1\sigma_t$  on a daily scale, reflecting the magnitude and consistency of the impact concurrently.

247 At the national total scale, prior tests ( $ef_{-10\%}$ ,  $-1\%$ ,  $thre_{40\%/60\%}$ , and 4 sectors) influence CO<sub>2</sub>  
 248 emissions consistently over time while leaving NO<sub>x</sub> emissions unaffected (Fig. 3). This occurs because these  
 249 tests only impact sectoral attribution and CO<sub>2</sub>-to-NO<sub>x</sub> emission ratios. Total NO<sub>x</sub> emissions are determined  
 250 in the top-down process before sectoral attribution, thus remaining unchanged (Fig. S1). However, sector-

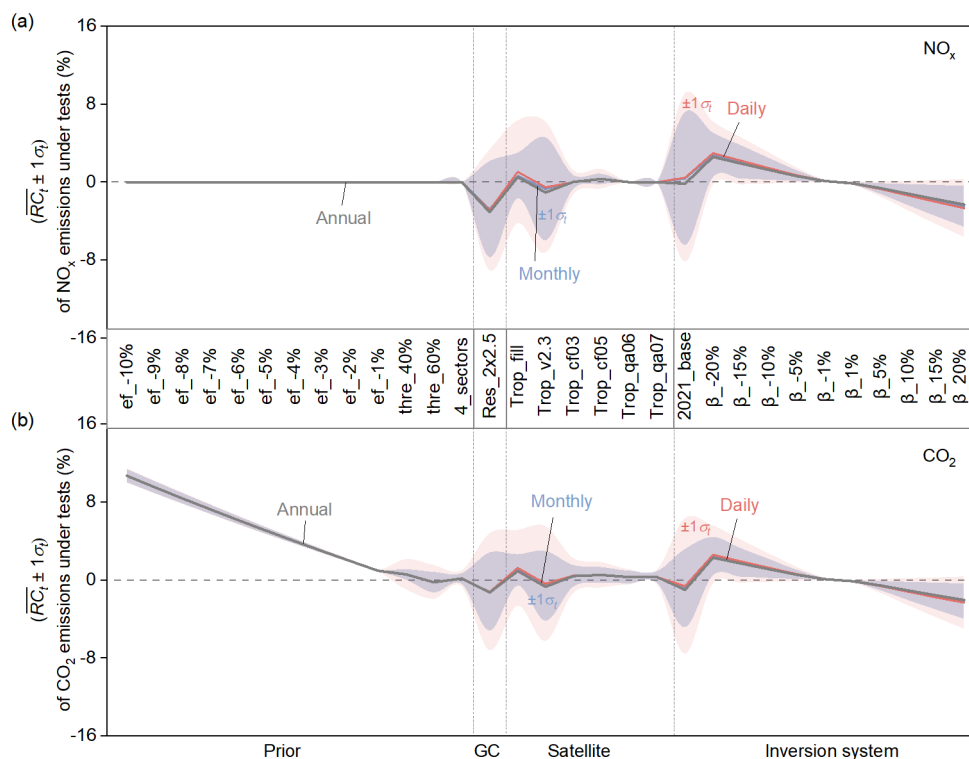


251 specific CO<sub>2</sub> emissions, derived from NO<sub>x</sub> emissions, are influenced due to the varying CO<sub>2</sub>-to-NO<sub>x</sub> emission  
252 ratios among sectors (Fig. S9). A reduction in NO<sub>x</sub> EFs increases  $r_{NO_x}$ , thereby increasing the sectoral CO<sub>2</sub>-  
253 to-NO<sub>x</sub> emission ratios since CO<sub>2</sub> EFs are assumed to be unchanged (Eq. 4). This results in a linear elevation  
254 of CO<sub>2</sub> emissions in tandem with the decreased NO<sub>x</sub> EFs (Fig. S5), with CO<sub>2</sub> emission variations reaching  
255 up to 10.7%±0.7% under  $ef_-10\%$ . Similarly, modifications in threshold values and sector classification alter  
256 the identification of dominant sectors per grid, changing the sectoral attribution.  $Thre_{40\%/60\%}$  and  
257  $4\_sectors$  bring about  $\overline{RC}_i \pm 1\sigma_i$  of 0.6%±1.5%, -0.2%±1.7%, and 0.2%±0.8% in CO<sub>2</sub> emissions, respectively,  
258 demonstrating their least influence on emission estimates. Despite differences in the magnitude of prior tests'  
259 impacts ( $\overline{RC}_i$ ), they share a consistency at finer temporal scales, with daily  $1\sigma_i$  below 4.0%.

260 Changes in model resolution (Res\_2×2.5) introduce the largest variation in estimates among all sensitivity  
261 tests, triggering  $\overline{RC}_i \pm 1\sigma_i$  of -1.2%±6.0% in daily CO<sub>2</sub> emissions. Its notable inconsistency of impact on the  
262 finer temporal scale ( $1\sigma_i > 4.0\%$ ) can be traced back to its induced spatiotemporally diverse changes in  $\beta$   
263 (Figs. S8a and S8b). The overall low estimate of  $\beta$  under Res\_2×2.5 results in negative  $RC_i$ , and the uneven  
264 spatial distribution of  $\beta$  explains the large  $1\sigma_i$ .

265 As for the impact of satellite constraint, the systematic changes such as missing value supplementation  
266 (Trop\_fill) or version changes (Trop\_v2.3) have a larger impact with daily CO<sub>2</sub> emission variations of  
267 1.3%±3.9% and -0.4%±5.9%, while alterations in satellite data quality screening conditions  
268 (Trop\_cf/Trop\_qa) exert a relatively minor impact on estimates with  $\overline{RC}_i \pm 1\sigma_i$  less than 0.5%±1.8%. The  
269 spatiotemporal changes in satellite NO<sub>2</sub> retrievals contribute to the inconsistent effects of Trop\_fill and  
270 Trop\_v2.3 on daily emissions. However, the small  $1\sigma_i$  in screening condition tests suggests that the  
271 uncertainty of satellite retrievals has a minor impact on estimates unless there are systematic changes,  
272 possibly because we used the ten-day moving average satellite observation data to constrain emissions.

273 Among inversion system parameters tests, the alteration of the reference year (2021\_base) exhibits a notable  
274 temporally inconsistent impact, with  $\overline{RC}_i \pm 1\sigma_i$  of -0.6%±6.9% in daily CO<sub>2</sub> emissions. This inconsistency  
275 can be attributed to the spatiotemporally diverse changes in  $\beta$ , similar to the model resolution test (Figs. S8c  
276 and S8d). In contrast, changes in  $\beta$  ( $\beta_{[-20\%, 20\%]}$ ) exert a more notable but consistent impact on estimates,  
277 linearly strengthening as the tested amplitude increases (Fig. S5), with  $\beta_{20\%}$  triggering variations of  
278 2.6%±3.0% in CO<sub>2</sub> emissions. The spatiotemporally uniform changes in  $\beta$  act linearly on the inversion  
279 estimate of NO<sub>x</sub> emissions (Eq. 1), and then on CO<sub>2</sub> emissions. Therefore, their impact remains consistent on  
280 a daily scale.



281

282 **Figure 3. Comparison of the impacts of various tests on national total (a) NO<sub>x</sub> and (b) CO<sub>2</sub> emissions**  
 283 **at different time scales.** Gray lines correspond to the  $\overline{RC}_i$  in annual emissions. Blue lines depict the average  
 284  $\overline{RC}_i$  in monthly emissions, with the blue shadow indicating monthly scale  $1\sigma_i$ . Red lines illustrate the average  
 285  $\overline{RC}_i$  in daily emissions, accompanied by the red shadow indicating daily scale  $1\sigma_i$ .

### 286 3.3 Emission sensitivity across source sectors

287 Regarding daily national sectoral NO<sub>x</sub> and CO<sub>2</sub> emissions, their responses to different sensitivity tests, in  
 288 terms of both emission magnitude and consistency ( $\overline{RC}_i \pm 1\sigma_i$ ), are largely similar, except for NO<sub>x</sub> EFs tests  
 289 (ef<sub>-</sub>[10%, -1%]) (Fig. 4). Therefore, we primarily discuss the impacts of tests on sectoral emissions using  
 290 CO<sub>2</sub> as a representative (refer to Text. S2 for discussion on sectoral NO<sub>x</sub> emission), and then delve into  
 291 elucidating the divergent impact of NO<sub>x</sub> EFs on sectoral NO<sub>x</sub> and CO<sub>2</sub> emissions.

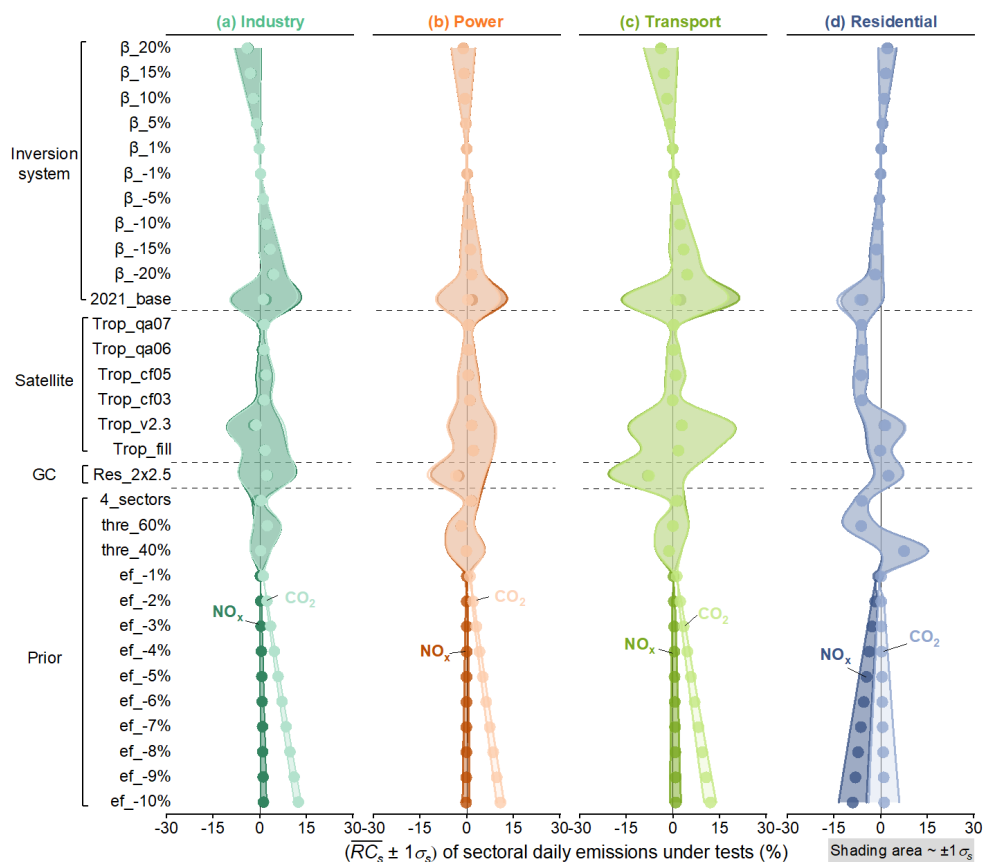
292 Irrespective of NO<sub>x</sub> emission factor changes (ef<sub>-</sub>[10%, -1%]), industrial and power emissions exhibit greater  
 293 robustness than transport and residential emissions, which are more susceptible to different configurations.  
 294 Specifically, residential emissions demonstrate the highest susceptibility to reference year, showing  
 295  $\overline{RC}_i \pm 1\sigma_i$  of up to  $-6.7\% \pm 7.3\%$  in CO<sub>2</sub> emissions in 2021\_base test, and exclusively display notable  
 296 sensitivity to prior tests (4\_sectors and thre\_40%/60%) compared to other sectors (Fig. 4). In contrast,  
 297 transport emissions are notably influenced by model resolution, with Res\_2x2.5 incurring CO<sub>2</sub> emission  
 298 variations of  $-7.8\% \pm 12.2\%$ . Among all sensitivity tests, the model resolution stands out as the most influential



299 factor on sectoral emissions, because the resolution of grid cells affects the determination of the dominant  
300 source sector.

301 The overall largest sensitivity of residential emissions to sensitivity tests is potentially attributed to its low  
302 proportion to total emissions (Fig. S10). Take `thre_40%/60%` as an example, lowering the threshold from 50%  
303 to 40% results in identifying more grids as residential source dominant. This, in turn, leads to an increase in  
304 residential emission proportions when allocating the total TROPOMI-constrained NO<sub>x</sub> emissions into sectors  
305 and subsequently CO<sub>2</sub> emissions. Conversely, fewer grids are assigned as residential-dominant when the  
306 threshold rises from 50% to 60%, resulting in lower residential emissions (Fig. S11). The next sensitive sector  
307 is transport, particularly vulnerable to mode resolution, which may be associated with its characteristics in  
308 spatial distribution. Transport-dominant grids, particularly those with truck emissions, are typically located  
309 close to industry-dominant grids whose NO<sub>x</sub> emissions outweigh those from the transport (Zheng et al., 2020).  
310 The use of a coarser horizontal resolution could result in a diminished attribution of emissions to transport.

311 The reduction in NO<sub>x</sub> EFs (`ef_-10%`, `-1%`) is the only test impacting sectoral NO<sub>x</sub> and CO<sub>2</sub> emissions  
312 differently. For NO<sub>x</sub> emissions, the residential sector shows the strongest sensitivity with  $\overline{RC_s} \pm 1\sigma_s$  of up to  
313  $-9.1\% \pm 4.5\%$  under `ef_-10%`. However, its influence on CO<sub>2</sub> emissions is most pronounced in all sectors  
314 except residential, with variations of  $12.4\% \pm 1.1\%$  in CO<sub>2</sub> emissions from industry,  $11.9\% \pm 1.9\%$  from  
315 transport,  $10.8\% \pm 1.2\%$  from power, but only  $1.0\% \pm 4.9\%$  from residential sectors under `ef_-10%`. The  
316 reduction in NO<sub>x</sub> EFs shifts the dominant sector attribution, substantially lowering NO<sub>x</sub> emissions from the  
317 residential sector due to its vulnerability to these changes, similar to the impact seen with the `thre_60%`. The  
318 other sectoral (industry, transport, and power) CO<sub>2</sub> emissions present stronger sensitivity to NO<sub>x</sub> EFs tests,  
319 linearly correlated with the extent of EFs changes. The decline in sectoral NO<sub>x</sub> EFs linearly reduces  $rNO_x$   
320 (Eq. 4), raising the corresponding CO<sub>2</sub> emissions by increasing sectoral CO<sub>2</sub>-to-NO<sub>x</sub> emission ratios.



321

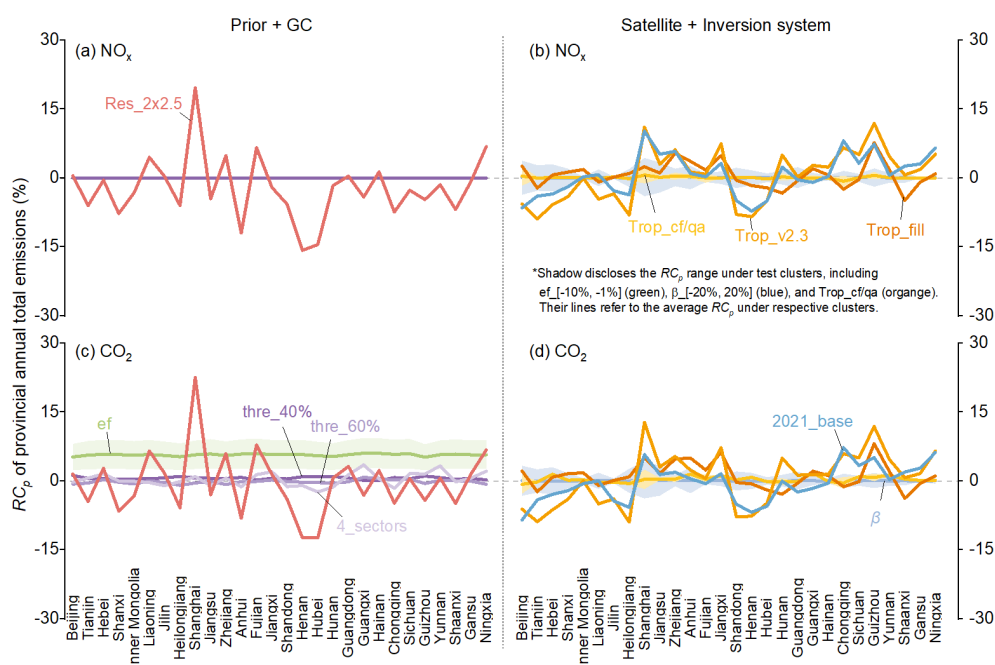
322 **Figure 4. Response of sectoral national NO<sub>x</sub> and CO<sub>2</sub> emissions to different sensitivity tests on a daily**  
 323 **scale.** From left to right, the panels correspond to the (a) industry, (b) power, (c) transport, and (d) residential  
 324 source sectors, as the label notes. The dots inside each figure are the average  $RC_s$  of daily NO<sub>x</sub> (deep color)  
 325 and CO<sub>2</sub> (light color) emissions incurred by corresponding tests. The shading area indicates the  $1\sigma_s$  of  
 326 daily sectoral emissions in different tests.

### 327 3.4 Emission sensitivity at subnational scales

328 Refining spatial coverage from national to subnational level (i.e., province) reveals that factors causing  
 329 inconsistent impacts over finer time scales also tend to induce inconsistent impacts on more granular spatial  
 330 regions (Fig. 5). On the annual total scales, the  $RC_p$  of NO<sub>x</sub> and CO<sub>2</sub> emissions at the provincial scale closely  
 331 resemble each other under most sensitivity tests, except for prior tests that only influence CO<sub>2</sub> emissions (Fig.  
 332 S13). When comparing across provinces, the sensitivity of emissions to tests correlates with the size of the  
 333 provincial area, with smaller regions exhibiting greater susceptibility. Shanghai, the smallest provincial-level  
 334 administrative unit in China in terms of area, experiences the largest  $RC_p$  throughout China in nearly all tests.  
 335 Conversely, Inner Mongolia, one of China's top three largest provinces, undergoes the minimum  $RC_p$  in all  
 336 tests. Under Res\_2×2.5, the  $RC_p$  of annual total NO<sub>x</sub> and CO<sub>2</sub> emissions in Shanghai are 19.6% and 22.6%,  
 337 respectively, while in Inner Mongolia, they are -3.2% and -3.3%. Employing a resolution of 2°×2.5° in



338 Shanghai is impractical in real-world applications, as it would result in fewer than two grids covering the  
 339 area. Henan also encounters substantial  $RC_p$  under Res\_2x2.5, reaching as high as -15.8% and -12.4% in  
 340 annual total  $\text{NO}_x$  and  $\text{CO}_2$  emissions. This could be attributed to its proximity to Shandong, a province with  
 341 approximately twice the emissions of Henan, making Henan particularly sensitive to the changes in model  
 342 resolution due to the overlapping grid cells. It is noteworthy that Guizhou exhibits the highest sensitivity to  
 343 satellite constraint, with  $RC_p$  reaching up to 11.9% and 11.8% in annual total  $\text{NO}_x$  and  $\text{CO}_2$  emissions under  
 344 Trop\_v2.3. This sensitivity is attributed to the high cloudiness of the Yunnan-Guizhou Plateau, causing  
 345 satellite observations to be highly uncertain over Guizhou (Wang et al., 2023; Li et al., 2021; Cai et al., 2022).



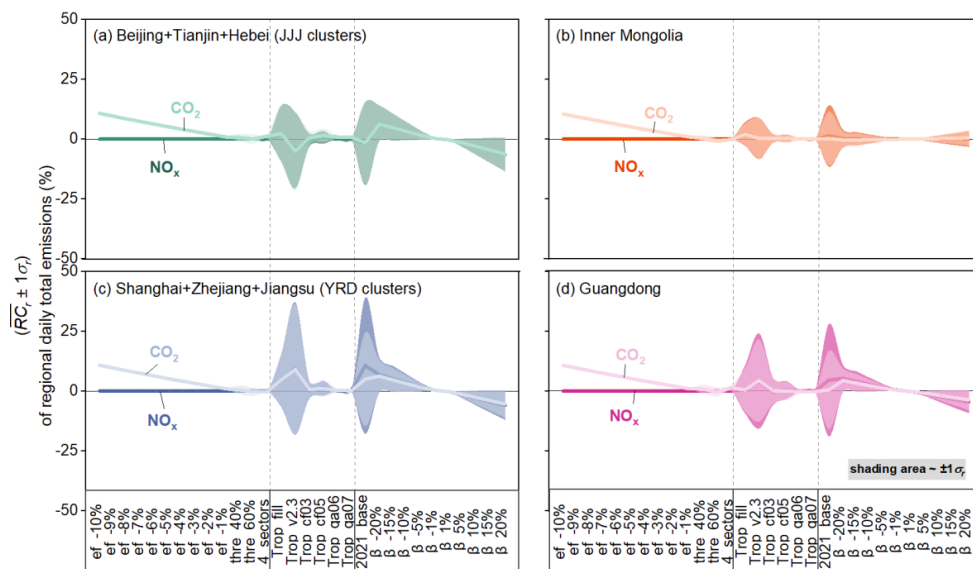
346

347 **Figure 5. Response of provincial annual total  $\text{NO}_x$  and  $\text{CO}_2$  emissions to different tests.** (a) and (b) show  
 348  $RC_p$  of  $\text{NO}_x$  emissions incurred by tests. (c) and (d) are plotted for  $\text{CO}_2$  emission as (a) and (b). Lines refer  
 349 to the  $RC_p$  caused by the corresponding test or the averaged  $RC_p$  caused by corresponding test clusters (ef\_[-  
 350 10%, -1%] and  $\beta$ [-20%, 20%]), and the shadow refers to the  $RC_p$  range in test clusters. Only provinces with  
 351 enough TROPOMI observations are shown here (i.e., grids with  $\text{NO}_2$  TVCDs larger than  $1 \times 10^{15}$   
 352 molecules/cm<sup>2</sup> cover more than 90% of anthropogenic  $\text{NO}_x$  emissions within provinces).

353 To further investigate the daily total emission response ( $\overline{RC}_i \pm 1\sigma_i$ ) to tests at the regional scale, we select  
 354 and analyze Jing-Jin-Ji clusters (JJJ, including Beijing, Tianjin, and Hebei), Inner Mongolia, Yangtze River  
 355 Delta clusters (YRD, including Shanghai, Zhejiang, and Jiangsu), and Guangdong (the location of the Pearl  
 356 River Delta). These regions respectively represent an industrialized region with high population density, an  
 357 industrialized region with sparse population density, and two major economic development zones with high  
 358 population density in China (Fig. 6). Geographically, these regions span North China (JJJ and Inner  
 359 Mongolia), East China (YRD), and South China (Guangdong), thereby covering different meteorological and



360 geographic factors. Overall, the  $\overline{RC_r} \pm 1\sigma_r$  of daily regional emissions are similar for NO<sub>x</sub> and CO<sub>2</sub> except for  
 361 ef<sub>[-10%, -1%]</sub>, resembling their daily national emission responses (Fig. 3). The  $\overline{RC_r} \pm 1\sigma_r$  of daily regional  
 362 emissions is especially notable in YRD and Guangdong (southern part of China). This could be attributed to  
 363 the relatively low NO<sub>2</sub> concentration in southern China (Fig. S2), making them particularly sensitive to spatial  
 364 variations in parameters, such as the  $\beta$  in 2021\_base (Fig. S8) and NO<sub>2</sub> TVCDs in Trop\_v2.3 test. Besides,  
 365 the cloud fraction is higher in southern China, introducing larger uncertainties in remote sensing (Liu et al.,  
 366 2019; Latsch et al., 2022). The emission responses to prior and  $\beta$ [-20%, 20%] tests are close for these four  
 367 regions, particularly in the prior tests, suggesting that these impacts on emissions are less dependent on  
 368 geographic factors.



369

370 **Figure 6. Response of regional total NO<sub>x</sub> and CO<sub>2</sub> emissions to tests on a daily scale.** (a), (b), (c), and (d)  
 371 show the  $\overline{RC_r} \pm 1\sigma_r$  of daily NO<sub>x</sub> (deep color) and CO<sub>2</sub> (light color) emissions in different tests in Jing-Jin-Ji  
 372 clusters (Beijing, Tianjin, and Hebei), Inner Mongolia, Yangtze River Delta clusters (Shanghai, Zhejiang,  
 373 and Jiangsu), and Guangdong. The shading area inside each figure refers to the corresponding  $1\sigma_r$ . It is worth  
 374 noting that the Res<sub>2×2.5</sub> test is not shown here since the resolution of 2°×2.5° proves too coarse for certain  
 375 regions, rendering it unrealistic for real-world applications. The result containing Res<sub>2×2.5</sub> is present in SI  
 376 as Fig. S14 for reference.

#### 377 4 Discussion

378 This study delineates an approximate spectrum of uncertainties inherent in deriving conclusions of varying  
 379 precision with our air pollution satellite sensor-based CO<sub>2</sub> emission inversion system. When interpreting  
 380 conclusions based on the emission data derived from such an inversion system, it is practical and imperative  
 381 to aggregate emissions across different dimensions to fulfill specific usage requirements. Direct utilization  
 382 of data with all fine-grained resolutions at temporal, sectoral, and spatial dimensions poses challenges. If





383 adhering to a variation tolerance of 5%, the reliability of annual national NO<sub>x</sub> and CO<sub>2</sub> emissions is  
384 established in most cases. Notably, careful attention is needed when selecting model resolution and attributing  
385 sectoral emissions. Expanding the tolerance to 10%, which is still below the conventional bottom-up method's  
386 uncertainty range of 13%-37% (Zhao et al., 2011; Huo et al., 2022), renders annual regional or daily national  
387 emissions robust from an average perspective. Nevertheless, meticulous scrutiny is advised when drawing  
388 conclusions based on daily sectoral or daily regional emissions, especially in specific regions (e.g., Shanghai,  
389 Guizhou). The large uncertainty of daily sectoral emission is typically observed in other emission datasets,  
390 such as Carbon Monitor (up to 40% uncertainty) (Liu et al., 2020c; Huo et al., 2022). Further liberalizing the  
391 tolerance to 25%, which is quite uncertain for scientific and policy-making purposes, the majority of  
392 conclusions derived from our estimates stand as reliable. The extensive tolerance range primarily stems from  
393 regional emissions, posing a challenging issue for many emission inversion techniques. For example, the  
394 uncertainty in NO<sub>x</sub> emissions derived from the 2D MISATEAM (chemical transport Model-Independent  
395 SATellite-derived Emission estimation Algorithm for Mixed-sources) method is approximately 20% for large  
396 and mid-size US cities (Liu et al., 2023), and the uncertainty for daily NO<sub>x</sub> and CO<sub>2</sub> emissions based on the  
397 superposition model ranges from 37% to 48% on a city scale (Zhang et al., 2023).

398 This study paves the way for the continuous improvement of the current air pollution satellite sensor-based  
399 CO<sub>2</sub> emission inversion system. Firstly, prioritizing a nimble and appropriate horizontal resolution is crucial  
400 for establishing accurate localized relationships between NO<sub>2</sub> TVCDs and NO<sub>x</sub> emissions, contributing to  
401 improved NO<sub>x</sub> and CO<sub>2</sub> emission estimations from temporal, sectoral, and spatial perspectives. Secondly, the  
402 more accurate satellite observation is conducive to reducing the uncertainty in final results, presenting  
403 increasing promise with advancements in remote sensing technology. Besides, the progress in multi-species  
404 synchronous observations through satellite and aircraft platforms offers alternative verification for multi-  
405 species emission inversion, such as the Copernicus Anthropogenic Carbon Dioxide Monitoring constellation  
406 (CO2M) (Sierk et al., 2021). Thirdly, the reliability of sectoral NO<sub>x</sub> EFs changes, which determine CO<sub>2</sub>-to-  
407 NO<sub>x</sub> emission ratios, is essential for the accurate conversion from NO<sub>x</sub> to CO<sub>2</sub> emissions. This underscores  
408 the need to acquire more accurate NO<sub>x</sub> EFs. While obtaining on-site measurements of CO<sub>2</sub>-to-NO<sub>x</sub> emission  
409 ratios is challenging, efforts are underway to enhance its configuration. An iterative modification of NO<sub>x</sub> EFs  
410 within the current system could be incorporated, minimizing the gap between bottom-up updated and  
411 TROPOMI-constrained sectoral NO<sub>x</sub> emissions to below 2%. This approach yields more accurate CO<sub>2</sub>-to-  
412 NO<sub>x</sub> emission ratios and CO<sub>2</sub> emissions (Fig. S15). The optimized CO<sub>2</sub> emission change from 2021 to 2022  
413 is +0.6%, reflecting a more precise representation of the growth in fossil fuel consumption (+1.9%). Fourthly,  
414 utilizing a more refined approach to determine dominant sectors at a grid level can reduce the uncertainty of  
415 small-contributing sectoral emissions, particularly in the residential sector. These enhancements will improve  
416 the system's accuracy in estimating emissions across all dimensions, positioning it as a valuable tool for  
417 simultaneous inversion-based monitoring of greenhouse gas and air pollutants emissions, ultimately  
418 supporting a strategic roadmap for the vision of clean air and climate warming mitigation.

419



420 *Code and data availability.* The source code of the GEOS-Chem model is available at  
421 <https://geoschem.github.io/>. The prior NO<sub>x</sub> and CO<sub>2</sub> emissions of 2019 MEIC (v1.4) are available at  
422 [http://meicmodel.org.cn/?page\\_id=541&lang=en](http://meicmodel.org.cn/?page_id=541&lang=en). The v2.4.0 TROPOMI NO<sub>2</sub> column concentrations are  
423 publicly available at [https://www.temis.nl/airpollution/no2col/no2regio\\_tropomi.php](https://www.temis.nl/airpollution/no2col/no2regio_tropomi.php). The activity level data  
424 of China from 2019 to 2022 including the industrial production of cement, iron, thermal electricity, etc., are  
425 available at <https://data.stats.gov.cn/english/easyquery.htm?cn=C01>.

426 *Supplement.* The supplement related to this article is available online.

427 *Author Contributions.* Bo Zheng designed the research and led the analysis. Hui Li performed the simulation,  
428 analyzed the data, and created the graphs. Bo Zheng, Jiaxin Qiu, and Hui Li wrote the manuscript.

429 *Competing interests.* The authors declare that they have no conflict of interest.

430 *Acknowledgements.* The authors thank the editor and the anonymous referees for helpful comments that have  
431 improved the paper.

432 *Financial support.* This work was supported by the National Natural Science Foundation of China (Grant No.  
433 42375096).



#### 434 References

- 435 Cai, D., Tao, L., Yang, X.-Q., Sang, X., Fang, J., Sun, X., Wang, W., and Yan, H.: A climate perspective of  
436 the quasi-stationary front in southwestern China: structure, variation and impact, *Climate Dynamics*, 59, 547-  
437 560, 10.1007/s00382-022-06151-1, 2022.
- 438 Cooper, M., Martin, R. V., Padmanabhan, A., and Henze, D. K.: Comparing mass balance and adjoint  
439 methods for inverse modeling of nitrogen dioxide columns for global nitrogen oxide emissions, *Journal of*  
440 *Geophysical Research: Atmospheres*, 122, 4718-4734, 10.1002/2016JD025985, 2017.
- 441 Cooper, M. J., Martin, R. V., Hammer, M. S., Levelt, P. F., Veeffkind, P., Lamsal, L. N., Krotkov, N. A.,  
442 Brook, J. R., and McLinden, C. A.: Global fine-scale changes in ambient NO<sub>2</sub> during COVID-19 lockdowns,  
443 *Nature*, 601, 380-387, 10.1038/s41586-021-04229-0, 2022.
- 444 Goldberg, D. L., Lu, Z., Oda, T., Lamsal, L. N., Liu, F., Griffin, D., McLinden, C. A., Krotkov, N. A., Duncan,  
445 B. N., and Streets, D. G.: Exploiting OMI NO<sub>2</sub> satellite observations to infer fossil-fuel CO<sub>2</sub> emissions from  
446 U.S. megacities, *Science of The Total Environment*, 695, 133805, 10.1016/j.scitotenv.2019.133805, 2019.
- 447 Guevara, M., Petetin, H., Jorba, O., Denier van der Gon, H., Kuenen, J., Super, I., Granier, C., Doumbia, T.,  
448 Ciais, P., Liu, Z., Lamboll, R. D., Schindlbacher, S., Matthews, B., and Pérez García-Pando, C.: Towards  
449 near-real-time air pollutant and greenhouse gas emissions: lessons learned from multiple estimates during the  
450 COVID-19 pandemic, *Atmospheric Chemistry and Physics*, 23, 8081-8101, 10.5194/acp-23-8081-2023,  
451 2023.
- 452 Hersbach, H., Bell, B., Berrisford, P., Hirahara, S., and Thépaut, J.: The ERA5 global reanalysis, *Quarterly*  
453 *Journal of the Royal Meteorological Society*, 2020.
- 454 Huo, D., Liu, K., Liu, J., Huang, Y., Sun, T., Sun, Y., Si, C., Liu, J., Huang, X., Qiu, J., Wang, H., Cui, D.,  
455 Zhu, B., Deng, Z., Ke, P., Shan, Y., Boucher, O., Darnet, G., Liang, G., Zhao, J., Chen, L., Zhang, Q., Ciais,  
456 P., Zhou, W., and Liu, Z.: Near-real-time daily estimates of fossil fuel CO<sub>2</sub> emissions from major high-  
457 emission cities in China, *Sci Data*, 9, 684, 10.1038/s41597-022-01796-3, 2022.
- 458 Ke, P., Deng, Z., Zhu, B., Zheng, B., Wang, Y., Boucher, O., Arous, S. B., Zhou, C., Andrew, R. M., Dou,  
459 X., Sun, T., Song, X., Li, Z., Yan, F., Cui, D., Hu, Y., Huo, D., Chang, J.-P., Engelen, R., Davis, S. J., Ciais,  
460 P., and Liu, Z.: Carbon Monitor Europe near-real-time daily CO<sub>2</sub> emissions for 27 EU countries and the  
461 United Kingdom, *Scientific Data*, 10, 374, 10.1038/s41597-023-02284-y, 2023.
- 462 Lamsal, L. N., Martin, R. V., Padmanabhan, A., van Donkelaar, A., Zhang, Q., Sioris, C. E., Chance, K.,  
463 Kurosu, T. P., and Newchurch, M. J.: Application of satellite observations for timely updates to global  
464 anthropogenic NO<sub>x</sub> emission inventories, *Geophysical Research Letters*, 38, 10.1029/2010gl046476, 2011.
- 465 Lange, K., Richter, A., Schönhardt, A., Meier, A. C., Bösch, T., Seyler, A., Krause, K., Behrens, L. K.,  
466 Wittrock, F., Merlaud, A., Tack, F., Fayt, C., Friedrich, M. M., Dimitropoulou, E., Van Roozendaal, M.,  
467 Kumar, V., Donner, S., Dörner, S., Lauster, B., Razi, M., Borger, C., Uhlmannsiek, K., Wagner, T., Ruhtz,  
468 T., Eskes, H., Bohn, B., Santana Diaz, D., Abuhassan, N., Schüttemeyer, D., and Burrows, J. P.: Validation  
469 of Sentinel-5P TROPOMI tropospheric NO<sub>2</sub> products by comparison with NO<sub>2</sub> measurements from airborne  
470 imaging DOAS, ground-based stationary DOAS, and mobile car DOAS measurements during the SSP-VAL-  
471 DE-Ruhr campaign, *Atmos. Meas. Tech.*, 16, 1357-1389, 10.5194/amt-16-1357-2023, 2023.
- 472 Latsch, M., Richter, A., Eskes, H., Sneep, M., Wang, P., Veeffkind, P., Lutz, R., Loyola, D., Argyrouli, A.,  
473 Valks, P., Wagner, T., Sihler, H., van Roozendaal, M., Theys, N., Yu, H., Siddans, R., and Burrows, J. P.:  
474 Intercomparison of Sentinel-5P TROPOMI cloud products for tropospheric trace gas retrievals, *Atmos. Meas.*  
475 *Tech.*, 15, 6257-6283, 10.5194/amt-15-6257-2022, 2022.
- 476 Le Quéré, C., Peters, G. P., Friedlingstein, P., Andrew, R. M., Canadell, J. G., Davis, S. J., Jackson, R. B.,  
477 and Jones, M. W.: Fossil CO<sub>2</sub> emissions in the post-COVID-19 era, *Nature Climate Change*, 11, 197-199,  
478 10.1038/s41558-021-01001-0, 2021.
- 479 Li, H., Zheng, B., Ciais, P., Boersma, K. F., Riess, T. C. V. W., Martin, R. V., Broquet, G., van der A, R., Li,  
480 H., Hong, C., Lei, Y., Kong, Y., Zhang, Q., and He, K.: Satellite reveals a steep decline in China's CO<sub>2</sub>  
481 emissions in early 2022, *Science Advances*, 9, eadg7429, 10.1126/sciadv.adg7429, 2023.
- 482 Li, J., Sun, Z., Liu, Y., You, Q., Chen, G., and Bao, Q.: Top-of-Atmosphere Radiation Budget and Cloud  
483 Radiative Effects Over the Tibetan Plateau and Adjacent Monsoon Regions From CMIP6 Simulations,  
484 *Journal of Geophysical Research: Atmospheres*, 126, e2020JD034345, 10.1029/2020JD034345, 2021.
- 485 Li, L., Zhang, Y., Zhou, T., Wang, K., Wang, C., Wang, T., Yuan, L., An, K., Zhou, C., and Lu, G.: Mitigation  
486 of China's carbon neutrality to global warming, *Nat Commun*, 13, 5315, 10.1038/s41467-022-33047-9, 2022.
- 487 Liu, F., Duncan, B. N., Krotkov, N. A., Lamsal, L. N., Beirle, S., Griffin, D., McLinden, C. A., Goldberg, D.  
488 L., and Lu, Z.: A methodology to constrain carbon dioxide emissions from coal-fired power plants using



- 489 satellite observations of co-emitted nitrogen dioxide, *Atmos. Chem. Phys.*, 20, 99-116, 10.5194/acp-20-99-  
490 2020, 2020a.
- 491 Liu, F., Beirle, S., Joiner, J., Choi, S., Tao, Z., Knowland, K. E., Smith, S. J., Tong, D. Q., Ma, S., Fasnacht,  
492 Z. T., and Wagner, T.: High-resolution Mapping of Nitrogen Oxide Emissions in Large US Cities from  
493 TROPOMI Retrievals of Tropospheric Nitrogen Dioxide Columns, *EGUsphere*, 2023, 1-18,  
494 10.5194/egusphere-2023-1842, 2023.
- 495 Liu, F., Page, A., Strode, S. A., Yoshida, Y., Choi, S., Zheng, B., Lamsal, L. N., Li, C., Krotkov, N. A., Eskes,  
496 H., van der A, R., Veeffkind, P., Levelt, P. F., Hauser, O. P., and Joiner, J.: Abrupt decline in tropospheric  
497 nitrogen dioxide over China after the outbreak of COVID-19, *Science Advances*, 6, eabc2992,  
498 10.1126/sciadv.abc2992, 2020b.
- 499 Liu, Y., Tang, Y., Hua, S., Luo, R., and Zhu, Q.: Features of the Cloud Base Height and Determining the  
500 Threshold of Relative Humidity over Southeast China, *Remote Sensing*, 11, 2900, 2019.
- 501 Liu, Z., Ciaia, P., Deng, Z., Lei, R., Davis, S. J., Feng, S., Zheng, B., Cui, D., Dou, X., Zhu, B., Guo, R., Ke,  
502 P., Sun, T., Lu, C., He, P., Wang, Y., Yue, X., Wang, Y., Lei, Y., Zhou, H., Cai, Z., Wu, Y., Guo, R., Han,  
503 T., Xue, J., Boucher, O., Boucher, E., Chevallier, F., Tanaka, K., Wei, Y., Zhong, H., Kang, C., Zhang, N.,  
504 Chen, B., Xi, F., Liu, M., Bréon, F.-M., Lu, Y., Zhang, Q., Guan, D., Gong, P., Kammen, D. M., He, K., and  
505 Schellnhuber, H. J.: Near-real-time monitoring of global CO<sub>2</sub> emissions reveals the effects of the COVID-19  
506 pandemic, *Nature Communications*, 11, 5172, 10.1038/s41467-020-18922-7, 2020c.
- 507 MacDonald, C. G., Mastrogiacomo, J. P., Laughner, J. L., Hedelius, J. K., Nassar, R., and Wunch, D.:  
508 Estimating enhancement ratios of nitrogen dioxide, carbon monoxide and carbon dioxide using satellite  
509 observations, *Atmos. Chem. Phys.*, 23, 3493-3516, 10.5194/acp-23-3493-2023, 2023.
- 510 Meinshausen, M., Lewis, J., McGlade, C., Gutschow, J., Nicholls, Z., Burdon, R., Cozzi, L., and Hackmann,  
511 B.: Realization of Paris Agreement pledges may limit warming just below 2 degrees C, *Nature*, 604, 304-  
512 309, 10.1038/s41586-022-04553-z, 2022.
- 513 Miyazaki, K. and Bowman, K.: Predictability of fossil fuel CO<sub>2</sub> from air quality emissions, *Nature*  
514 *Communications*, 14, 1604, 10.1038/s41467-023-37264-8, 2023.
- 515 Nassar, R., Hill, T. G., McLinden, C. A., Wunch, D., Jones, D. B. A., and Crisp, D.: Quantifying CO<sub>2</sub>  
516 Emissions From Individual Power Plants From Space, *Geophysical Research Letters*, 44, 10,045-010,053,  
517 10.1002/2017GL074702, 2017.
- 518 Reuter, M., Buchwitz, M., Schneising, O., Krautwurst, S., O'Dell, C. W., Richter, A., Bovensmann, H., and  
519 Burrows, J. P.: Towards monitoring localized CO<sub>2</sub> emissions from space: co-located regional CO<sub>2</sub> and NO<sub>2</sub>  
520 enhancements observed by the OCO-2 and S5P satellites, *Atmos. Chem. Phys.*, 19, 9371-9383, 10.5194/acp-  
521 19-9371-2019, 2019.
- 522 Shan, Y., Ou, J., Wang, D., Zeng, Z., Zhang, S., Guan, D., and Hubacek, K.: Impacts of COVID-19 and fiscal  
523 stimuli on global emissions and the Paris Agreement, *Nature Climate Change*, 11, 200-206, 10.1038/s41558-  
524 020-00977-5, 2021.
- 525 Sierk, B., Fernandez, V., Bézy, J.-L., Meijer, Y., Durand, Y., Bazalgette Courrèges-Lacoste, G., Pachot, C.,  
526 Löscher, A., Nett, H., Minoglou, K., Boucher, L., Windpassinger, R., Pasquet, A., Serre, D., and te Hennepe,  
527 F.: The Copernicus CO<sub>2</sub>M mission for monitoring anthropogenic carbon dioxide emissions from space,  
528 *International Conference on Space Optics — ICSO 2021*, SPIE2021.
- 529 Turner, A. J., Henze, D. K., Martin, R. V., and Hakami, A.: The spatial extent of source influences on modeled  
530 column concentrations of short-lived species, *Geophysical Research Letters*, 39, 10.1029/2012GL051832,  
531 2012.
- 532 van Geffen, J., Eskes, H., Compernelle, S., Pinardi, G., Verhoelst, T., Lambert, J. C., Sneep, M., ter Linden,  
533 M., Ludewig, A., Boersma, K. F., and Veeffkind, J. P.: Sentinel-5P TROPOMI NO<sub>2</sub> retrieval: impact of  
534 version v2.2 improvements and comparisons with OMI and ground-based data, *Atmos. Meas. Tech.*, 15,  
535 2037-2060, 10.5194/amt-15-2037-2022, 2022.
- 536 Wang, Z., Zhang, M., Li, H., Wang, L., Gong, W., and Ma, Y.: Bias correction and variability attribution  
537 analysis of surface solar radiation from MERRA-2 reanalysis, *Climate Dynamics*, 10.1007/s00382-023-  
538 06873-w, 2023.
- 539 Wei, J., Liu, S., Li, Z., Liu, C., Qin, K., Liu, X., Pinker, R. T., Dickerson, R. R., Lin, J., Boersma, K. F., Sun,  
540 L., Li, R., Xue, W., Cui, Y., Zhang, C., and Wang, J.: Ground-Level NO<sub>2</sub> Surveillance from Space Across  
541 China for High Resolution Using Interpretable Spatiotemporally Weighted Artificial Intelligence, *Environ*  
542 *Sci Technol*, 56, 9988-9998, 10.1021/acs.est.2c03834, 2022.
- 543 Wren, S. N., McLinden, C. A., Griffin, D., Li, S.-M., Cober, S. G., Darlington, A., Hayden, K., Mihele, C.,  
544 Mittermeier, R. L., Wheeler, M. J., Wolde, M., and Liggio, J.: Aircraft and satellite observations reveal



545 historical gap between top-down and bottom-up CO<sub>2</sub> emissions from Canadian oil sands, *PNAS Nexus*, 2,  
546 10.1093/pnasnexus/pgad140, 2023.  
547 Yang, E. G., Kort, E. A., Ott, L. E., Oda, T., and Lin, J. C.: Using Space-Based CO<sub>2</sub> and NO<sub>2</sub> Observations  
548 to Estimate Urban CO<sub>2</sub> Emissions, *Journal of Geophysical Research: Atmospheres*, 128, e2022JD037736,  
549 10.1029/2022JD037736, 2023.  
550 Zhang, Q., Boersma, K. F., Zhao, B., Eskes, H., Chen, C., Zheng, H., and Zhang, X.: Quantifying daily NO<sub>x</sub>  
551 and CO<sub>2</sub> emissions from Wuhan using satellite observations from TROPOMI and OCO-2, *Atmos. Chem.*  
552 *Phys.*, 23, 551-563, 10.5194/acp-23-551-2023, 2023.  
553 Zhang, Q., Zheng, Y., Tong, D., Shao, M., Wang, S., Zhang, Y., Xu, X., Wang, J., He, H., Liu, W., Ding, Y.,  
554 Lei, Y., Li, J., Wang, Z., Zhang, X., Wang, Y., Cheng, J., Liu, Y., Shi, Q., Yan, L., Geng, G., Hong, C., Li,  
555 M., Liu, F., Zheng, B., Cao, J., Ding, A., Gao, J., Fu, Q., Huo, J., Liu, B., Liu, Z., Yang, F., He, K., and Hao,  
556 J.: Drivers of improved PM<sub>2.5</sub> air quality in China from 2013 to 2017, *Proc Natl Acad Sci USA*, 116, 24463-  
557 24469, 10.1073/pnas.1907956116, 2019.  
558 Zhao, Y., Nielsen, C. P., Lei, Y., McElroy, M. B., and Hao, J.: Quantifying the uncertainties of a bottom-up  
559 emission inventory of anthropogenic atmospheric pollutants in China, *Atmos. Chem. Phys.*, 11, 2295-2308,  
560 10.5194/acp-11-2295-2011, 2011.  
561 Zheng, B., Geng, G., Ciais, P., Davis, S. J., Martin, R. V., Meng, J., Wu, N., Chevallier, F., Broquet, G.,  
562 Boersma, F., van der A, R., Lin, J., Guan, D., Lei, Y., He, K., and Zhang, Q.: Satellite-based estimates of  
563 decline and rebound in China's CO<sub>2</sub> emissions during COVID-19 pandemic, *Science Advances*, 6, eabd4998,  
564 10.1126/sciadv.abd4998, 2020.  
565 Zheng, B., Tong, D., Li, M., Liu, F., Hong, C., Geng, G., Li, H., Li, X., Peng, L., Qi, J., Yan, L., Zhang, Y.,  
566 Zhao, H., Zheng, Y., He, K., and Zhang, Q.: Trends in China's anthropogenic emissions since 2010 as the  
567 consequence of clean air actions, *Atmos. Chem. Phys.*, 18, 14095-14111, 10.5194/acp-18-14095-2018, 2018.

568